ORIGINAL ARTICLE

lajss.org
Latin American Journal of Solids and Structures

www.lajss.org

Dynamic Response of a Nearly Saturated Half-Space Containing a Circular-Arc Canyon under Plane P-Wave Excitation

Jinbo Chen[a], Bin Hou[a], Xiangdong Zhao[a], Wenwen Li[a], Feng Liu[a*]

[a] Gansu Forestry Voctech University, Tianshui 741020, China. Email: chenjinbolzjtu@163.com, houb1016@163.com, gsts_zhao@163.com, 632148632@qq.com, zmr2026@163.com

* Corresponding author

https://doi.org/10.1590/1679-7825/e9098

Abstract

This study investigates plane P-wave scattering by a circular-arc canyon in a nearly saturated soil half-space. An analytical model is established based on Biot's two-phase poroelastic theory and the homogeneous-fluid assumption. Surface displacement amplitudes are obtained using Fourier–Bessel series expansions and a large-arc approximation. The solution is verified by convergence analysis and by reducing the formulation to the saturated case for comparison with published results. Parametric analyses clarify the effects of saturation, incident angle, depth-to-width ratio, dimensionless frequency, and porosity on horizontal and vertical surface responses. The results show that saturation mainly affects the response near full saturation, while the two displacement components exhibit different sensitivities to incident angle. Larger depth-to-width ratios and higher dimensionless frequencies enhance canyon-induced scattering, whereas increasing porosity generally reduces displacement amplitudes. The findings provide a theoretical basis for seismic response evaluation of nearly saturated sites with circular-arc canyons.

Keywords

Biot poroelasticity; homogeneous pore fluid; Fourier–Bessel series; large-arc approximation; topographic amplification

Graphical Abstract

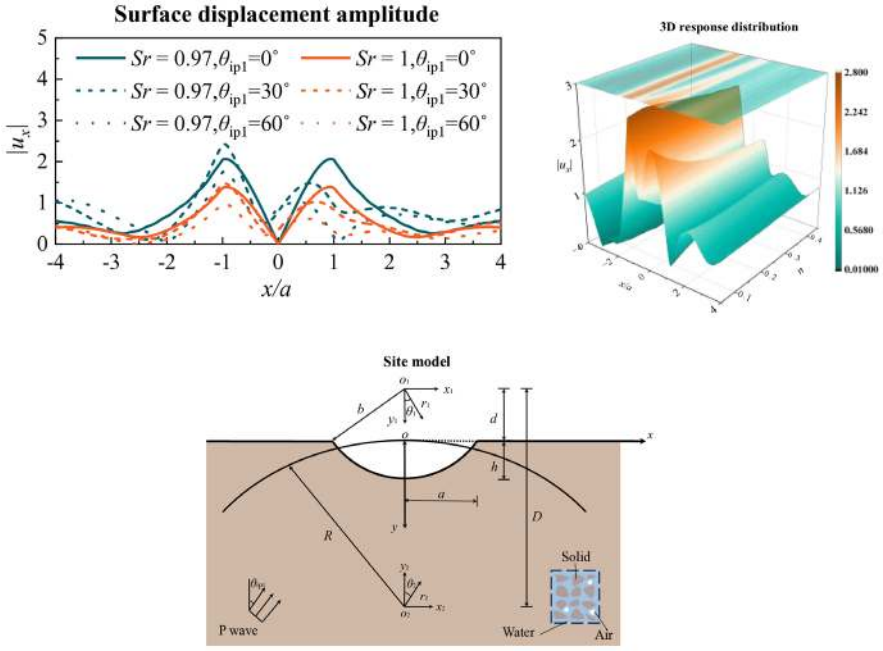

Received April 26, 2026. In revised form June 16, 2026. Accepted July 14, 2026. Available online July 16, 2026.
https://doi.org/10.1590/1679-7825/e9098

Latin American Journal of Solids and Structures. ISSN 1679-7825. Copyright © **2026**. This is an Open Access article distributed under the terms of the Creative Commons Attribution license, which permits unrestricted use, distribution, and reproduction in any medium, provided the original work is properly cited.

1 INTRODUCTION

Local site effects strongly influence seismic ground motions and remain important in geotechnical earthquake engineering. Observations and theoretical studies indicate that, beyond subsurface conditions, surface topography can alter wave propagation and ground-motion distribution, affecting slopes, dam foundations, canyon bridges, and mountain infrastructure (Sanchez-Sesma 1987; Geli et al. 1988; Weber et al. 2022). Unlike horizontally layered sites, depressions, canyons, and valleys induce two-dimensional scattering, diffraction, and mode conversion, leading to stronger local amplification and frequency-dependent site response (Shi et al. 2026; Ma et al. 2025a; Weber et al. 2022; Ma et al. 2025b).

Considerable effort has been devoted to plane P- and SV-wave scattering by depressed topography in single-phase elastic half-spaces. Early studies on circular cylindrical canyons with different depth-to-width ratios showed that incident angle, frequency, and geometry strongly affect surface displacement, and that ground motion may depart markedly from the free-field response when the topographic scale is comparable to the wavelength (Lee and Cao 1989; Cao and Lee 1990). Later, the problem was extended to valleys of arbitrary shape, where weighted-residual solutions demonstrated that irregular geometries amplify spatially nonuniform surface motion (Lee and Wu 1994). Subsequent work on semicircular valleys and circular-arc canyons improved wave-function expansions and traction-free boundary treatment, leading to more accurate solutions for P/SV-wave scattering, especially at higher frequencies (Lee and Liu 2014). Despite these advances, most studies remain within the single-phase elastic framework and therefore cannot represent solid–fluid coupling in real soils.

Natural soils are porous media, and pore fluids can strongly influence their dynamic behavior. Biot's theory for saturated porous media provided the foundation for wave propagation analysis under fluid–solid coupling conditions (Biot 1956). Later developments in homogenization and multiphase porous-medium theory further extended this framework (Liu et al. 2026; Liu et al. 2020; Feng and Xu 2025). Accordingly, topographic scattering problems were gradually extended from single-phase elastic media to saturated porous half-spaces. For depressed topography in saturated porous media, previous studies used the Fourier–Bessel series expansion and the indirect boundary element method to examine the effects of incident angle, frequency, porosity, and drainage conditions on surface displacement distributions (Li and Zhao 2005; Ba et al. 2010; You et al. 2011; Huang et al. 2022). More recently, complex-variable approaches have also been introduced to investigate the surface response of semicircular canyons in saturated half-spaces under incident P/SV waves (Jin et al. 2024; Jin et al. 2023; Zhang et al. 2022; Lainer and Müller 2026). These studies indicate that once pore-fluid effects are included, surface displacement amplitudes, peak–valley locations, and parameter sensitivity may differ markedly from predictions based on single-phase elastic models. This underscores the need to investigate topographic scattering within a porous-medium framework.

Compared with fully saturated soils, a large proportion of near-surface soils encountered in engineering practice are actually in a nearly saturated state, namely, a highly saturated condition that is not fully saturated. Although such soils contain only a small amount of gas in their pores, their dynamic behavior may differ substantially from that of fully saturated soils. Vardoulakis and Beskos (1986) were among the first to establish a dynamic model for nearly saturated porous media and showed that changes in saturation can significantly affect body-wave propagation characteristics. Subsequent studies addressing wave transmission and mechanical response in partly saturated or highly saturated porous media further demonstrated that even limited pore gas can markedly alter the effective compressibility of the medium, thereby influencing compressional-wave velocity, attenuation behavior, and mode-conversion characteristics (Degrande et al. 1998; Li et al. 2018; Zhang and Ping 2018). Research on dynamic responses under highly saturated or nearly saturated conditions has since been extended to lined cavities, layered foundations, seismic responses of seabeds, and fluid-porous medium interface effects, consistently indicating that even slight changes in saturation may still lead to pronounced response differences as the soil approaches full saturation (Wang et al. 2015; Chen et al. 2020; Li et al. 2024). This implies that, if the particular nature of nearly saturated media is neglected, the actual wave response of near-surface sites may not be properly characterized in studies of topographic effects.

Overall, previous studies have provided important theoretical bases for wave scattering by depressed topography in elastic and saturated porous half-spaces, and significant progress has also been made in wave propagation in nearly saturated porous media. Despite these advances, the analytical treatment of P-wave scattering by circular-arc canyons in nearly saturated half-spaces remains limited. Existing elastic canyon-scattering solutions generally ignore solid–fluid coupling, whereas saturated poroelastic canyon models usually assume fully water-filled pores and cannot capture the marked change in equivalent pore-fluid compressibility caused by a small amount of occluded gas. Meanwhile, studies on nearly saturated porous media have mainly focused on body-wave propagation, layered foundations, lined cavities, seabed response, and fluid–porous medium interfaces, rather than the two-dimensional scattering and surface amplification induced by circular-arc depressed topography. Therefore, the combined influence of near-saturation-dependent pore-fluid compressibility and circular-arc canyon scattering under incident P waves has not been fully characterized within an analytical framework.

Against this background, this study develops a Fourier–Bessel analytical solution for plane P-wave scattering by a circular-arc canyon in a nearly saturated poroelastic half-space by combining Biot's theory, the homogeneous-fluid assumption, and the large-arc approximation. Distinct from previous elastic or fully saturated porous models, the present formulation represents the water–air mixture in the pores through a saturation-dependent equivalent bulk modulus, while simultaneously satisfying the traction-free conditions on the canyon boundary and the approximated free surface. On this basis, the effects of saturation, incident angle, depth-to-width ratio, dimensionless frequency, and porosity on the horizontal and vertical surface displacement amplitudes are systematically examined. The results are expected to provide a theoretical reference for seismic response evaluation of nearly saturated sites with depressed topographic irregularities.

2 Governing equation

2.1 *Mathematical model*

Figure 1 illustrates the mathematical model. The rectangular coordinate systems (x,y),(x_1,y_1), and (x_2,y_2), together with the cylindrical coordinate systems(r_1,ϑ_1) and (r_2,ϑ_2), are defined in the figure. The depression has half-width a and depth h. The circular arc is centered at o_1 with radius b, and the distance from o_1 to the ground surface is d. Different canyon profiles can be represented by varying the depth ratio h/a.

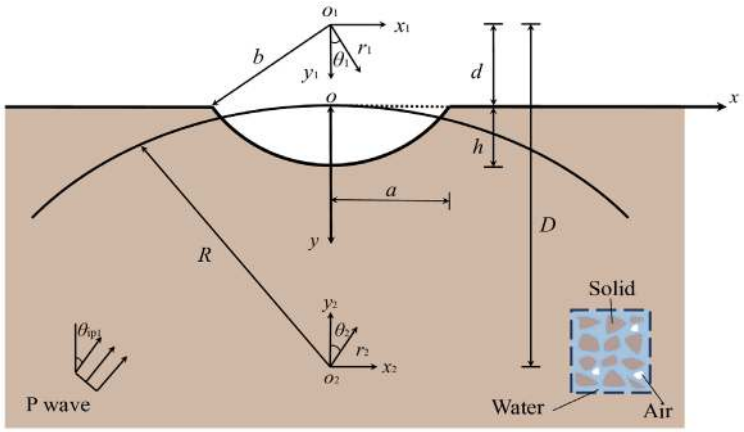

Figure 1 Site model of the circular-arc canyon with solid–water–air inset.

2.2 *Wave equation*

The nearly saturated half-space is composed of three phases, namely soil particles, air, and water. Their volumetric proportions are characterized by the porosity $n$and the degree of saturation S_r, defined as follows:

$$n = \frac{V_v}{V_t},\ S_r = \frac{V_W}{V_v} \tag{1}$$

where V_v is the pore volume, V_t is the total soil volume, and V_W represents the pore-fluid volume.

For a nearly saturated porous medium, the pore fluid is regarded as a mixture of water and air, in which the air exists in the form of occluded bubbles within the pore fluid. Therefore, it can be approximately treated as a homogeneous pore fluid. Its bulk modulus can be expressed as

$$K_f = \frac{1}{\frac{1}{K_l} + \frac{1 - S_r}{p_a}} \tag{2}$$

where K_f is the bulk modulus of the pore fluid, K_l is the bulk modulus of pore water, and p_a is the absolute pore pressure.

The governing equations for the nearly saturated porous medium are given by

$$\mu\nabla^2 u^{\mathrm{s}} + \mathrm{grad}[(\mu \ + \lambda \ + \alpha^2 M)\theta] - \mathrm{grad}(\alpha M\zeta) = \rho \ \ddot{u}^{\mathrm{s}} + \rho^{\mathrm{f}}\ddot{u}^{\mathrm{f}} \tag{3}$$

$$\alpha M\nabla\left(\nabla\cdot\boldsymbol{u}\right) + M\nabla\left(\nabla\cdot\boldsymbol{w}\right) = \rho_f\ddot{\boldsymbol{u}} + m\ddot{\boldsymbol{w}} + \beta\dot{\boldsymbol{w}} \tag{4}$$

where $\boldsymbol{u}$ and $\boldsymbol{w}$ denote the displacement of the solid skeleton and the fluid, respectively. λ and μ are the Lamé constants. The parameter $\beta = \eta_f / k_p$ denotes the viscous coupling coefficient between the pore fluid and the solid skeleton, where η_f is the dynamic viscosity of the pore fluid and k_p is the permeability coefficient. The parameters α and M in Biot's theory account, where $\alpha = 1 - K/K_s$ and $1/M = (\alpha - n)/K_s + n/K_f$. K, K_s and K_f represent the bulk moduli of the solid skeleton, solid particles, and pore fluid, respectively. The parameter $m = \rho_f/n$ is related to the mass density of the pore water and the geometric characteristics of the pores. The mass density of the mixture medium is given by $\rho = \left(1-n\right)\rho_s + n\rho_f$, where ρ_s and ρ_f are the densities of the solid and liquid phases, respectively.

Based on the Helmholtz vector decomposition:

$$\boldsymbol{u} = \nabla\varphi_s + \nabla\times\psi_s, \boldsymbol{w} = \nabla\varphi_f + \nabla\times\psi_f \tag{5}$$

For an incident P_1 wave with circular frequency ω and incident angle θ_{ip1}, the potential function in the (x, y) coordinate system is

$$\varphi_{\mathrm{i}}^{\alpha}\left(x,y\right) = \exp\left[\mathrm{i}k_{\mathrm{ip1}}\left(x\sin\theta_{\mathrm{ip1}} - y\cos\theta_{\mathrm{ip1}}\right) - \mathrm{i}\omega t\right] \tag{6}$$

where ω is the circular frequency, θ_{ip1} is the incident angle of the P_1 wave, and k_{ip1} is the corresponding incident P_1-wave number.

In the absence of the circular-arc canyon, the plane free surface of the nearly saturated half-space generates reflected P_1, P_2, and S waves. Their potential functions are expressed as follows:

$$\varphi_{\mathrm{rp1}}^{\alpha}\left(x,y\right) = A_{\mathrm{rp1}}^{\alpha}\exp\left[\mathrm{i}k_{\mathrm{rp1}}\left(x\sin\theta_{\mathrm{rp1}} + y\cos\theta_{\mathrm{rp1}}\right)\right] \tag{7}$$

$$\varphi_{\mathrm{rp2}}^{\alpha}\left(x,y\right) = A_{\mathrm{rp2}}^{\alpha}\exp\left[\mathrm{i}k_{\mathrm{rp2}}\left(x\sin\theta_{\mathrm{rp2}} + y\cos\theta_{\mathrm{rp2}}\right)\right] \tag{8}$$

$$\psi_{\mathrm{rs}}^{\alpha}\left(x,y\right) = B_{\mathrm{rs}}^{\alpha}\exp\left[\mathrm{i}k_{\mathrm{rs}}\left(x\sin\theta_{\mathrm{rs}} + y\cos\theta_{\mathrm{rs}}\right)\right] \tag{9}$$

where k_{rp1}, k_{rp2}, and k_{rs} are the wave numbers of the reflected P_1, P_2, and S waves, respectively; θ_{rp1}, θ_{rp2}, and θ_{rs} are the corresponding reflection angles; and $A_{\mathrm{rp1}}^{\alpha}$, $A_{\mathrm{rp2}}^{\alpha}$, and B_{rs}^{α} are the corresponding amplitude coefficients.

3 Solution of the Problem

Eqs. (7)–(9) are rewritten in cylindrical coordinates and expanded as follows:

$$\varphi_{\mathrm{i+rp1}}^{\alpha}\left(r_1,\theta_1\right) = \sum_{n=0}^{\infty} J_n\left(k_{\mathrm{ip1}}r_1\right)\left(C_{01,n}\cos n\theta_1 + D_{01,n}\sin n\theta_1\right) \tag{10}$$

$$\varphi_{\mathrm{rp2}}^{\alpha}\left(r_1,\theta_1\right)=\sum_{n=0}^{\infty}J_n\left(k_{\mathrm{rp2}}r_1\right)\left(C_{02,n}\cos n\theta_1+D_{02,n}\sin n\theta_1\right) \tag{11}$$

$$\psi_{\mathrm{rs}}^{\alpha}\left(r_1,\theta_1\right)=\sum_{n=0}^{\infty}J_n\left(k_{\mathrm{rs}}r_1\right)\left(C_{03,n}\sin n\theta_1+D_{03,n}\cos n\theta_1\right) \tag{12}$$

Here, ε_n is the Fourier expansion coefficient, where $\varepsilon_0=1$ and $\varepsilon_n=2$ for $n\geq 1$. The signs in the exponential terms are determined by the propagation directions of the incident and reflected waves. The coefficients are given by

$$C_{01,n}=\varepsilon_n \mathrm{i}^n\cos n\theta_{\mathrm{ip1}}\left[\left(-1\right)^n\exp\left(\mathrm{i}dk_{\mathrm{ip1}}\cos\theta_{\mathrm{ip1}}\right)+A_{\mathrm{rp1}}^{\alpha}\exp\left(\text{-}\mathrm{i}dk_{\mathrm{ip1}}\cos\theta_{\mathrm{ip1}}\right)\right],$$

$$D_{01,n}=\varepsilon_n \mathrm{i}^n\sin n\theta_{\mathrm{ip1}}\left[-\left(-1\right)^n\exp\left(\mathrm{i}dk_{\mathrm{ip1}}\cos\theta_{\mathrm{ip1}}\right)+A_{\mathrm{rp1}}^{\alpha}\exp\left(\text{-}\mathrm{i}dk_{\mathrm{ip1}}\cos\theta_{\mathrm{ip1}}\right)\right],$$

$$C_{02,n}=A_{\mathrm{rp2}}^{\alpha}\varepsilon_n \mathrm{i}^n\cos n\theta_{\mathrm{rp2}}\exp\left(\text{-}\mathrm{i}dk_{\mathrm{rp2}}\cos\theta_{\mathrm{rp2}}\right),$$

$$D_{02,n}=A_{\mathrm{rp2}}^{\alpha}\varepsilon_n \mathrm{i}^n\sin n\theta_{\mathrm{rp2}}\exp\left(\text{-}\mathrm{i}dk_{\mathrm{rp2}}\cos\theta_{\mathrm{rp2}}\right),$$

$$C_{03,n}=B_{\mathrm{rs}}^{\alpha}\varepsilon_n \mathrm{i}^n\sin n\theta_{\mathrm{rs}}\exp\left(\text{-}\mathrm{i}dk_{\mathrm{rs}}\cos\theta_{\mathrm{rs}}\right),$$

$$D_{03,n}=B_{\mathrm{rs}}^{\alpha}\varepsilon_n \mathrm{i}^n\cos n\theta_{\mathrm{rs}}\exp\left(\text{-}\mathrm{i}dk_{\mathrm{rs}}\cos\theta_{\mathrm{rs}}\right).$$

Because the wave potentials are expressed in the (r_1,ϑ_1) system, the boundary conditions at y=0 cannot be imposed directly. Following Shi et al. (2026), Lee and Cao (1989), and Cao and Lee (1990), the half-space surface is approximated by a circular arc of radius R centered at o_2. The resulting solution is approximate, and the error is negligible when $R>>b$ (e.g., R>50b).

Accordingly, the scattered P_1, P_2, and S waves generated by the circular-arc canyon and by the large circular-arc approximation can be expanded into Fourier–Bessel series as follows:

$$\varphi_{\mathrm{dp1}}^{\alpha}\left(r_1,\theta_1\right)=\sum_{n=0}^{\infty}H_n^{(1)}\left(k_{\mathrm{rp1}}r_1\right)\left(C_{11,n}^{(1)}\cos n\theta_1+D_{11,n}^{(1)}\sin n\theta_1\right) \tag{13}$$

$$\varphi_{\mathrm{dp2}}^{\alpha}\left(r_1,\theta_1\right)=\sum_{n=0}^{\infty}H_n^{(1)}\left(k_{\mathrm{rp2}}r_1\right)\left(C_{12,n}^{(1)}\cos n\theta_1+D_{12,n}^{(1)}\sin n\theta_1\right) \tag{14}$$

$$\psi_{\mathrm{ds}}^{\alpha}\left(r_1,\theta_1\right)=\sum_{n=0}^{\infty}H_n^{(1)}\left(k_{\mathrm{rs}}r_1\right)\left(C_{13,n}^{(1)}\sin n\theta_1+D_{13,n}^{(1)}\cos n\theta_1\right) \tag{15}$$

$$\varphi_{\mathrm{ap1}}^{\alpha}\left(r_2,\theta_2\right)=\sum_{m=0}^{\infty}J_m\left(k_{\mathrm{rp1}}r_2\right)\left(C_{21,m}^{(2)}\cos m\theta_2+D_{21,m}^{(2)}\sin m\theta_2\right) \tag{16}$$

$$\varphi_{\mathrm{ap2}}^{\alpha}\left(r_2,\theta_2\right)=\sum_{m=0}^{\infty}J_m\left(k_{\mathrm{rp2}}r_2\right)\left(C_{22,m}^{(2)}\cos m\theta_2+D_{22,m}^{(2)}\sin m\theta_2\right) \tag{17}$$

$$\psi_{\mathrm{as}}^{\alpha}\left(r_2,\theta_2\right)=\sum_{m=0}^{\infty}J_m\left(k_{\mathrm{rs}}r_2\right)\left(C_{23,m}^{(2)}\sin m\theta_2+D_{23,m}^{(2)}\cos m\theta_2\right) \tag{18}$$

where $J_m(\ )$ and $H_n^{(1)}(\ )$ denote the first-kind Bessel and Hankel functions, respectively. In the (r_1,ϑ_1) system, the scattered P_1, P_2, and S waves are outgoing cylindrical waves from o_1; in the (r_2,ϑ_2) system, they represent reflected cylindrical waves between $r_1 = b$ and $r_2 = R$, satisfying the Sommerfeld radiation condition. Hence, the total wave potentials in the half-space are

$$\varphi^{\alpha} = \varphi_{\mathrm{i}}^{\alpha} + \varphi_{\mathrm{rp1}}^{\alpha} + \varphi_{\mathrm{rp2}}^{\alpha} + \varphi_{\mathrm{dp1}}^{\alpha} + \varphi_{\mathrm{dp2}}^{\alpha} + \varphi_{\mathrm{ap1}}^{\alpha} + \varphi_{\mathrm{ap2}}^{\alpha} \tag{19}$$

$$\psi^{\alpha} = \psi_{\mathrm{rs}}^{\alpha} + \psi_{\mathrm{ds}}^{\alpha} + \psi_{\mathrm{as}}^{\alpha} \tag{20}$$

Using Graf's addition theorem (Ma et al. 2023), Eqs. (13)–(18) can be transformed into the other coordinate system:

$$\varphi_{\mathrm{dp1}}^{\alpha}\left(r_2,\theta_2\right) = \sum_{m=0}^{\infty} J_m\left(k_{\mathrm{rp1}} r_2\right)\left(C_{11,m}^{(2)}\cos m\theta_2 + D_{11,m}^{(2)}\sin m\theta_2\right) \tag{21}$$

$$\varphi_{\mathrm{dp2}}^{\alpha}\left(r_2,\theta_2\right) = \sum_{m=0}^{\infty} J_m\left(k_{\mathrm{rp2}} r_2\right)\left(C_{12,m}^{(2)}\cos m\theta_2 + D_{12,m}^{(2)}\sin m\theta_2\right) \tag{22}$$

$$\psi_{\mathrm{ds}}^{\alpha}\left(r_2,\theta_2\right) = \sum_{m=0}^{\infty} J_m\left(k_{\mathrm{rs}} r_2\right)\left(C_{14,m}^{(2)}\sin m\theta_2 + D_{14,m}^{(2)}\cos m\theta_2\right) \tag{23}$$

$$\varphi_{\mathrm{ap1}}^{\alpha}\left(r_1,\theta_1\right) = \sum_{n=0}^{\infty} J_n\left(k_{\mathrm{rp1}} r_1\right)\left(C_{21,n}^{(1)}\cos n\theta_1 + D_{21,n}^{(1)}\sin n\theta_1\right) \tag{24}$$

$$\varphi_{\mathrm{ap2}}^{\alpha}\left(r_1,\theta_1\right) = \sum_{n=0}^{\infty} J_n\left(k_{\mathrm{rp2}} r_1\right)\left(C_{22,n}^{(1)}\cos n\theta_1 + D_{22,n}^{(1)}\sin n\theta_1\right) \tag{25}$$

$$\psi_{\mathrm{as}}^{\alpha}\left(r_1,\theta_1\right) = \sum_{n=0}^{\infty} J_n\left(k_{\mathrm{rs}} r_1\right)\left(C_{24,n}^{(1)}\sin n\theta_1 + D_{24,n}^{(1)}\cos n\theta_1\right) \tag{26}$$

where

$$\begin{bmatrix} C_{11,m}^{(2)} \\ C_{12,m}^{(2)} \\ D_{13,m}^{(2)} \end{bmatrix} = \sum_{n=0}^{\infty} \begin{bmatrix} F2_{nm}^{+}\left(k_{\mathrm{rp1}} D\right) & & \\ & F2_{nm}^{+}\left(k_{\mathrm{rp2}} D\right) & \\ & & F2_{nm}^{+}\left(k_{\mathrm{rs}} D\right) \end{bmatrix} \begin{bmatrix} C_{11,n}^{(1)} \\ C_{12,n}^{(1)} \\ D_{13,n}^{(1)} \end{bmatrix} \tag{27}$$

$$\begin{bmatrix} D_{11,m}^{(2)} \\ D_{12,m}^{(2)} \\ C_{13,m}^{(2)} \end{bmatrix} = \sum_{n=0}^{\infty} \begin{bmatrix} F2_{nm}^{-}\left(k_{\mathrm{rp1}} D\right) & & \\ & F2_{nm}^{-}\left(k_{\mathrm{rp2}} D\right) & \\ & & F2_{nm}^{-}\left(k_{\mathrm{rs}} D\right) \end{bmatrix} \begin{bmatrix} D_{11,n}^{(1)} \\ D_{12,n}^{(1)} \\ C_{13,n}^{(1)} \end{bmatrix} \tag{28}$$

$$\begin{bmatrix} C_{21,n}^{(1)} \\ C_{22,n}^{(1)} \\ D_{24,n}^{(1)} \end{bmatrix} = \sum_{n=0}^{\infty} \begin{bmatrix} F1_{nm}^{+}\left(k_{\mathrm{rp1}}D\right) & & \\ & F1_{nm}^{+}\left(k_{\mathrm{rp2}}D\right) & \\ & & F1_{nm}^{+}\left(k_{\mathrm{rs}}D\right) \end{bmatrix} \begin{bmatrix} C_{21,m}^{(2)} \\ C_{22,m}^{(2)} \\ D_{23,m}^{(2)} \end{bmatrix} \tag{29}$$

$$\begin{bmatrix} D_{21,n}^{(1)} \\ D_{22,n}^{(1)} \\ C_{24,n}^{(1)} \end{bmatrix} = \sum_{n=0}^{\infty} \begin{bmatrix} F1_{nm}^{-}\left(k_{\mathrm{rp1}}D\right) & & \\ & F1_{nm}^{-}\left(k_{\mathrm{rp2}}D\right) & \\ & & F1_{nm}^{-}\left(k_{\mathrm{rs}}D\right) \end{bmatrix} \begin{bmatrix} D_{21,m}^{(2)} \\ D_{22,m}^{(2)} \\ C_{24,m}^{(2)} \end{bmatrix} \tag{30}$$

In which

$$F2_{nm}^{\pm}\left(kD\right) = \frac{1}{2}\varepsilon_m\left[H_{n+m}\left(kD\right) \pm \left(-1\right)^m H_{n-m}\left(kD\right)\right], F1_{nm}^{\pm}\left(kD\right) = \frac{1}{2}\varepsilon_n\left[J_{n+m}\left(kD\right) \pm \left(-1\right)^m J_{n-m}\left(kD\right)\right]$$

$$F1_{nm}^{\pm}\left(kD\right) = \frac{1}{2}\varepsilon_n\left[J_{n+m}\left(kD\right) \pm \left(-1\right)^m J_{n-m}\left(kD\right)\right],.$$

The boundary are:

at the free surface y=0: $\sigma_{yy}^{S} = 0, \sigma_{xy}^{S} = 0, \sigma_{yy}^{f} = 0$ (31)

at the circular-arc boundary r_1=b: $\sigma_{rr}^{S} = 0, \sigma_{r\theta}^{S} = 0, \sigma_{rr}^{f} = 0$ (32)

at the circular-arc boundary r_2=R: $\sigma_{rr}^{S} = 0, \sigma_{r\theta}^{S} = 0, \sigma_{rr}^{f} = 0$ (33)

The stress and displacement components can be expressed in terms of the potential functions as follows:

$$\left.\begin{aligned} \sigma_{zz}^{s} &= \lambda\left(\frac{\partial^2\varphi_s}{\partial x^2} + \frac{\partial^2\varphi_s}{\partial z^2}\right) + 2\mu\left(\frac{\partial^2\varphi_s}{\partial z^2} + \frac{\partial^2\psi_s}{\partial x\partial z}\right) - \alpha p_f \\ \sigma_{xz}^{s} &= \mu\left(2\frac{\partial^2\varphi_s}{\partial x\partial z} + \frac{\partial^2\psi_s}{\partial x^2} - \frac{\partial^2\psi_s}{\partial z^2}\right) \\ \sigma_{zz}^{f} &= -\left[\alpha M\left(\frac{\partial^2\varphi_s}{\partial x^2} + \frac{\partial^2\varphi_s}{\partial z^2}\right) + M\left(\frac{\partial^2\varphi_f}{\partial x^2} + \frac{\partial^2\varphi_f}{\partial z^2}\right)\right] \\ u_x^s &= \frac{\partial\varphi_s}{\partial x} - \frac{\partial\psi_s}{\partial z}, u_z^s = \frac{\partial\varphi_s}{\partial z} + \frac{\partial\psi_s}{\partial x} \\ u_x^f &= \frac{\partial\varphi_f}{\partial x} - \frac{\partial\psi_f}{\partial z}, u_z^f = \frac{\partial\varphi_f}{\partial z} + \frac{\partial\psi_f}{\partial x} \end{aligned}\right\} \tag{34}$$

The corresponding expressions in cylindrical coordinates can be obtained accordingly.

$$\left.\begin{aligned}
\sigma_{yy}^{s} &= \lambda\left(\frac{\partial^2\varphi^{\mathrm{S}}}{\partial r^2}+\frac{1}{r}\frac{\partial\varphi^{\mathrm{S}}}{\partial r}+\frac{1}{r^2}\frac{\partial^2\varphi^{\mathrm{S}}}{\partial\theta^2}\right)+2\mu\left(\frac{\partial^2\varphi^{\mathrm{S}}}{\partial r^2}+\frac{1}{r}\frac{\partial^2\psi^{\mathrm{S}}}{\partial r\partial\theta}-\frac{1}{r^2}\frac{\partial\psi^{\mathrm{S}}}{\partial\theta}\right)-\alpha\sigma_{yy}^{f}\\
\sigma_{xy}^{s} &= \mu\left[2\left(\frac{1}{r}\frac{\partial^2\varphi^{S}}{\partial r\partial\theta}-\frac{1}{r^2}\frac{\partial\varphi^{S}}{\partial\theta}\right)+\frac{1}{r^2}\frac{\partial^2\psi^{S}}{\partial\theta^2}+\frac{1}{r}\frac{\partial\psi^{S}}{\partial r}-\frac{\partial^2\psi^{S}}{\partial r^2}\right]\\
\sigma_{yy}^{f} &= -M(\frac{\partial^2\varphi^{f}}{\partial r^2}+\frac{1}{r}\frac{\partial\varphi^{f}}{\partial r}+\frac{1}{r^2}\frac{\partial^2\varphi^{f}}{\partial\theta^2})-M\alpha\left(\frac{\partial^2\varphi^{\mathrm{S}}}{\partial r^2}+\frac{1}{r}\frac{\partial\varphi^{\mathrm{S}}}{\partial r}+\frac{1}{r^2}\frac{\partial^2\varphi^{\mathrm{S}}}{\partial\theta^2}\right)\\
u_r^{\mathrm{S}} &= \frac{\partial\varphi^{\mathrm{S}}}{\partial r}+\frac{1}{r}\frac{\partial\psi^{\mathrm{S}}}{\partial\theta},u_\theta^{\mathrm{S}}=\frac{1}{r}\frac{\partial\varphi^{\mathrm{S}}}{\partial\theta}-\frac{\partial\psi^{\mathrm{S}}}{\partial r}\\
u_r^{\mathrm{f}} &= \frac{\partial\varphi^{\mathrm{f}}}{\partial r}+\frac{1}{r}\frac{\partial\psi^{\mathrm{f}}}{\partial\theta},u_\theta^{\mathrm{f}}=\frac{1}{r}\frac{\partial\varphi^{\mathrm{f}}}{\partial\theta}-\frac{\partial\psi^{\mathrm{f}}}{\partial r}
\end{aligned}\right\} \tag{35}$$

Substituting Eqs. (16)–(18) and Eqs. (21)–(24) into boundary condition (33) gives

$$\begin{aligned}
&\sum_{m=0}^{\infty}\begin{bmatrix}E_{111}^{s(1)}(m,R) & E_{112}^{s(1)}(m,R) & E_{113}^{s(1)+}(m,R)\\ E_{211}^{s(1)-}(m,R) & E_{212}^{s(1)-}(m,R) & E_{213}^{s(1)}(m,R)\\ E_{311}^{s(1)}(m,R) & E_{312}^{s(1)}(m,R) & 0\end{bmatrix}\begin{Bmatrix}C_{11,m}^{(2)}+C_{21,m}^{(2)}\\ C_{12,m}^{(2)}+C_{22,m}^{(2)}\\ C_{13,m}^{(2)}+C_{23,m}^{(2)}\end{Bmatrix}\begin{Bmatrix}\cos m\theta_2\\ \sin m\theta_2\\ \cos m\theta_2\end{Bmatrix}+\\
&\sum_{m=0}^{\infty}\begin{bmatrix}E_{111}^{s(1)}(m,R) & E_{112}^{s(1)}(m,R) & E_{113}^{s(1)-}(m,R)\\ E_{211}^{s(1)+}(m,R) & E_{212}^{s(1)+}(m,R) & E_{213}^{s(1)}(m,R)\\ E_{311}^{s(1)}(m,R) & E_{312}^{s(1)}(m,R) & 0\end{bmatrix}\begin{Bmatrix}D_{11,m}^{(2)}+D_{21,m}^{(2)}\\ D_{12,m}^{(2)}+D_{22,m}^{(2)}\\ D_{13,m}^{(2)}+D_{23,m}^{(2)}\end{Bmatrix}\begin{Bmatrix}\sin m\theta_2\\ \cos m\theta_2\\ \sin m\theta_2\end{Bmatrix}=\begin{Bmatrix}0\\0\\0\\0\end{Bmatrix}
\end{aligned} \tag{36}$$

where

$$\begin{aligned}
&E_{11j}^{s(1)}(m,R)=\left[-k_{rpj}^2r^2\left(M\alpha^2+M\alpha m_j+\lambda+2\mu\right)+2\mu(m^2+m)\right]C_n^{(i)}\left(k_{rpj}r\right)-2\mu k_{rpj}rC_{n-1}^{(i)}\left(k_{rpj}r\right),\\
&E_{113}^{s(1)\mp}(m,R)=\mp2n\mu\left[-(m+1)C_n^{(i)}\left(k_{rs}r\right)+k_{rs}rC_{n-1}^{(i)}\left(k_{rs}r\right)\right],\\
&E_{213}^{s(1)}(m,R)=\mu\left[\left(-2m^2-2m+k_{rs}^2r^2\right)C_n^{(i)}\left(k_{rs}r\right)+2k_{rs}rC_{n-1}^{(i)}\left(k_{rs}r\right)\right],\\
&E_{21j}^{s(1)\mp}(m,R)=\mp2n\mu\left[-(m+1)C_n^{(i)}\left(k_{rpj}r\right)+k_{rpj}C_{n-1}^{(i)}\left(k_{rpj}r\right)\right],E_{31j}^{s(1)}(m,R)=Mk_{rpj}^2(\alpha+m_j)C_n^{(i)}\left(k_{rpj}r\right).
\end{aligned}$$

When $i=1$, $C_n^{(i)}(x)$ denotes the Bessel function $J_n(x)$; when $i=3$, $C_n^{(i)}(x)$ denotes the Hankel function $H_n^{(1)}(x)$.

Substituting Eqs. (10)–(12), Eqs. (13)–(15), and Eqs. (25)–(26) into boundary condition (32) yields:

$$\begin{aligned}
&\sum_{n=0}^{\infty}\begin{bmatrix}E_{111}^{s(3)}(n,b) & E_{112}^{s(3)}(n,b) & E_{113}^{s(3)+}(n,b)\\ E_{211}^{s(3)-}(n,b) & E_{212}^{s(3)-}(n,b) & E_{213}^{s(3)}(n,b)\\ E_{311}^{s(3)}(n,b) & E_{312}^{s(3)}(n,b) & 0\end{bmatrix}\begin{Bmatrix}C_{11,n}^{(1)}\\ C_{12,n}^{(1)}\\ C_{13,n}^{(1)}\end{Bmatrix}\begin{Bmatrix}\cos n\theta_1\\ \sin n\theta_1\\ \cos n\theta_1\end{Bmatrix}+\\
&\sum_{n=0}^{\infty}\begin{bmatrix}E_{111}^{s(1)}(n,b) & E_{112}^{s(1)}(n,b) & E_{113}^{s(1)+}(n,b)\\ E_{211}^{s(1)-}(n,b) & E_{212}^{s(1)-}(n,b) & E_{213}^{s(1)}(n,b)\\ E_{311}^{s(1)}(n,b) & E_{312}^{s(1)}(n,b) & 0\end{bmatrix}\begin{Bmatrix}C_{21,n}^{(1)}+C_{01,n}\\ C_{22,n}^{(1)}+C_{02,n}\\ C_{23,n}^{(1)}+C_{03,n}\end{Bmatrix}\begin{Bmatrix}\cos n\theta_1\\ \sin n\theta_1\\ \cos n\theta_1\end{Bmatrix}+\\
&\sum_{n=0}^{\infty}\begin{bmatrix}E_{111}^{s(3)}(n,b) & E_{112}^{s(3)}(n,b) & E_{113}^{s(3)-}(n,b)\\ E_{211}^{s(3)+}(n,b) & E_{212}^{s(3)+}(n,b) & E_{213}^{s(3)}(n,b)\\ E_{311}^{s(3)}(n,b) & E_{312}^{s(3)}(n,b) & 0\end{bmatrix}\begin{Bmatrix}D_{11,n}^{(1)}\\ D_{12,n}^{(1)}\\ D_{13,n}^{(1)}\end{Bmatrix}\begin{Bmatrix}\sin n\theta_1\\ \cos n\theta_1\\ \sin n\theta_1\end{Bmatrix}+\\
&\sum_{n=0}^{\infty}\begin{bmatrix}E_{111}^{s(1)}(n,b) & E_{112}^{s(1)}(n,b) & E_{113}^{s(1)-}(n,b)\\ E_{211}^{s(1)+}(n,b) & E_{212}^{s(1)+}(n,b) & E_{213}^{s(1)}(n,b)\\ E_{311}^{s(1)}(n,b) & E_{312}^{s(1)}(n,b) & 0\end{bmatrix}\begin{Bmatrix}D_{21,n}^{(1)}+D_{01,n}\\ D_{22,n}^{(1)}+D_{02,n}\\ D_{23,n}^{(1)}+D_{03,n}\end{Bmatrix}\begin{Bmatrix}\sin n\theta_1\\ \cos n\theta_1\\ \sin n\theta_1\end{Bmatrix}=\begin{Bmatrix}0\\0\\0\end{Bmatrix}
\end{aligned} \tag{37}$$

By combining Eqs. (36) and (37), the solutions of the wave-field potential functions can be obtained.

4 Discussion

4.1 *Verification*

The following dimensionless frequency is introduced:

$$\Omega = 2a/\lambda_S \tag{38}$$

where λ_S is the wavelength of the shear wave, and Ω denotes the dimensionless frequency.

To ensure the reliability of the subsequent numerical results, the convergence of the truncated Fourier–Bessel series is first examined. Following the treatment commonly adopted in scattering problems of circular-arc depressed topography, convergence is checked using the Cauchy criterion. For an arbitrary spatial point (r_1, ϑ_1), the difference between two successive truncations is calculated as

$$e\left(n;\, r_1,\, \theta_1\right) = \left| u\left(n+1;\, r_1,\, \theta_1\right) - u\left(n;\, r_1,\, \theta_1\right) \right| \tag{39}$$

where $e\left(n;\, r_1,\, \theta_1\right)$ denotes the difference in displacement response between two successive truncation orders, $\varepsilon = 10^{-6}$ is the convergence tolerance, and n_c is the minimum truncation order satisfying the convergence criterion. In the numerical examples, the convergence errors of the horizontal and vertical components are denoted by e_x and e_y, respectively.

When $n>n_c$ and $e\left(n;\, r_1,\, \theta_1\right) \le \varepsilon$, the series is regarded as convergent, and n_c denotes the required truncation number. The variations of e_x and e_y with the truncation number n are shown in Figure 2. It can be seen that, as n increases, the errors in both directions decay rapidly and become stable after a relatively small number of terms, indicating that the Fourier–Bessel series adopted in this study converges well. Therefore, in the following numerical calculations, the truncation number satisfying the required accuracy is used to ensure both the stability and efficiency of the computation.

After the convergence check, the proposed method is further validated against published results. For this purpose, the nearly saturated model is reduced to the saturated case, with Ω =1, $\theta_{ip1} = 0^{\circ}$, and the other parameters taken from Ba et al. (2010). Figure 3 compares the surface displacement amplitudes obtained here with those reported by Ba et al. The two sets of results agree well in overall trend, peak position, and amplitude level, confirming the validity of the present formulation and implementation.

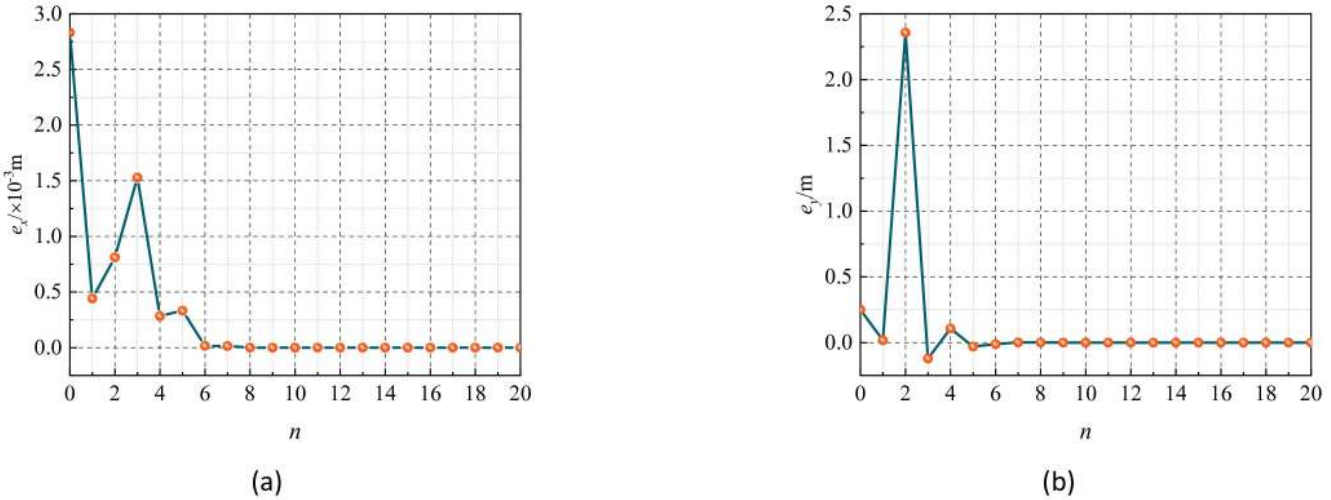

Figure 2 Convergence of the truncated Fourier–Bessel series with increasing truncation number n: (a) horizontal displacement error e_x; (b) vertical displacement error e_y.

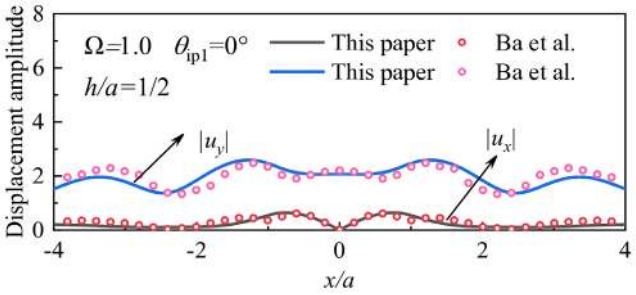

Figure 3 Validation against Ba et al. (2010) for the saturated case (Ω=1.0, θ_{ip1}=0°, h/a=1/2)

4.2 *Influence of saturation*

To examine the influence of saturation on P-wave scattering in a nearly saturated half-space with a circular-arc canyon, the material parameters listed in Table 1 are used (Yang et al. 1996). Figure 4 presents the surface displacement amplitudes for ϑ_{ip1}=30°, Ω=1, *n*=0.4, and *h*/*a*=0.5, with *Sr* varying from 0.97 to 1.00.

As shown in Fig. 4, the displacement response changes only slightly when *Sr* increases from 0.97 to 0.99, indicating weak sensitivity within the highly saturated range. However, when *Sr*=1.00, both horizontal and vertical displacement amplitudes decrease noticeably. The peak and trough positions remain almost unchanged, suggesting that the canyon geometry mainly controls the spatial distribution, whereas saturation mainly affects the response amplitude.

This variation is related to the pore-fluid bulk modulus. For *Sr*=0.97–0.99, a small amount of occluded gas remains in the pores, and the pore fluid is still relatively compressible. When *Sr*=1.00, the gas phase disappears and the pore fluid becomes purely liquid, increasing the bulk modulus and reducing the overall compressibility. Consequently, the scattering and local amplification near the canyon are weakened.

Table 1. Physical and mechanical parameters (Yang et al. 1996)

Material parameters	Permeability coefficient	Density of soil particle	Density of liquid	Dynamic viscosity of pore fluid	Bulk modulus of soil particles	Bulk modulus of liquid	Solid Skeleton Bulk Modulus
Symbol (unit)	k_p (m/s)	ρ_s (Kg/m³)	ρ_f (Kg/m³)	η_f (Pa•s)	K_s (GPa)	K_f (GPa)	K (MPa)
Magnitude	1×10^{-12}	2650	1000	1×10^{-3}	36	2	43
Material parameters	Lamé constant	Lamé constant					
Symbol (unit)	λ (GPa)	μ (GPa)					
Magnitude	2.62	2.61					

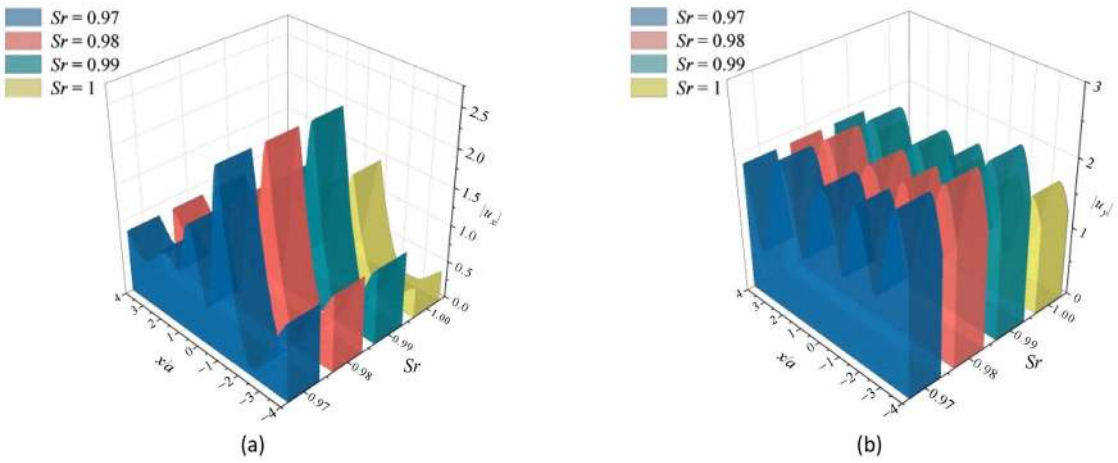

Figure 4 Influence of saturation on surface displacement amplitudes for θ_{ip1}=30°, Ω=1, n=0.4, and h/a=0.5: (a) $|u_x|$; (b) $|u_y|$.

4.3 *Influence of incident angle*

Figure 5 compares the displacement amplitudes for S_r=0.97 and S_r=1.00 at ϑ_{ip1}=0°, 30°, and 60°; the remaining parameters are the same as those in Section 4.2.

As shown in Fig. 5(a), the incident angle has a significant but non-monotonic effect on the horizontal displacement amplitude $|u_x|$. For both saturation states, $|u_x|$ is relatively small near the canyon center and larger near the two sides, indicating stronger local scattering around the depression boundaries. When S_r=0.97, a higher local peak appears at ϑ_{ip1}= 30°, whereas the overall amplitude decreases at ϑ_{ip1}= 60°. For S_r=1.00, the curves at 0° and 30° are close, while the response at 60° is clearly smaller.

The vertical displacement amplitude $|u_y|$ shows a more regular trend, as shown in Fig. 5(b). For both S_r=0.97 and S_r=1.00, $|u_y|$ decreases as the incident angle increases, with the largest response at 0° and the smallest response at 60°. The peak and trough positions change only slightly, suggesting that the incident angle mainly affects the amplitude level of $|u_y|$. At the same incident angle, the nearly saturated case generally gives larger displacement amplitudes than the fully saturated case, indicating a stronger scattering response under nearly saturated conditions.

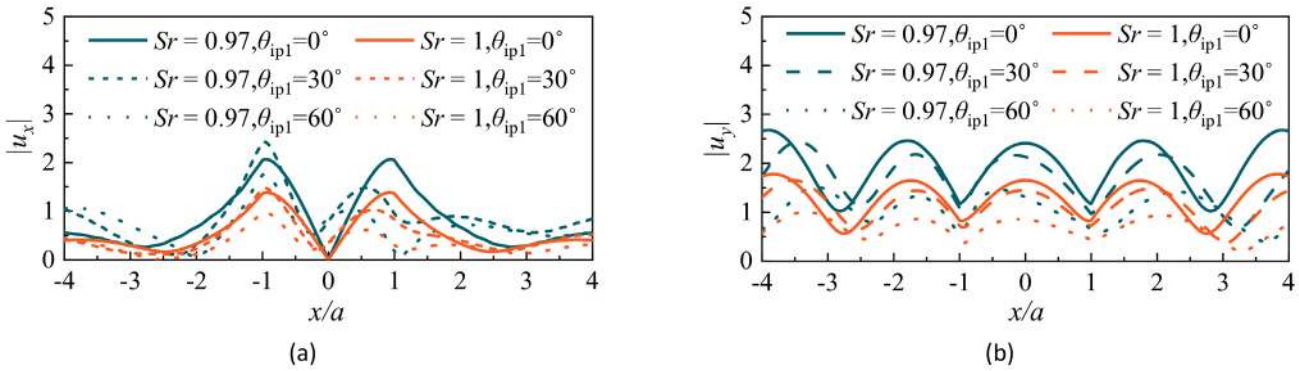

Figure 5 Influence of incident angle on surface displacement amplitudes for Sr=0.97 and Sr=1.00 (Ω=1, n=0.4, and h/a=0.5): (a) |ux|; (b) |uy|.

4.4 *Influence of depth-to-width*

Figure 6 compares the displacement amplitudes for S_r=0.97 and ϑ_{ip1}=0° as h/a increases from 0.25 to 1.00; the other parameters are the same as those in Section 4.2.

As shown in Fig. 6(a), the horizontal displacement amplitude $|u_x|$ is small and relatively smooth at h/a=0.25. With increasing h/a, the double-peak pattern near the canyon sides becomes more evident, and pronounced local peaks appear around x/a=±1. The largest local peak occurs at h/a=0.75. When h/a further increases to 1.00, the response remains relatively large, but the peak value no longer increases noticeably.

For the vertical displacement amplitude $|u_y|$ in Fig. 6(b), the influence of h/a is more direct. As h/a increases, the overall amplitude becomes larger and the curve becomes more oscillatory. The vertical response is weak at h/a=0.25, whereas larger h/a values lead to clearer peaks and troughs. The curves for h/a=0.75 and 1.00 are close, indicating that the amplification effect tends to slow down when the canyon becomes sufficiently deep.

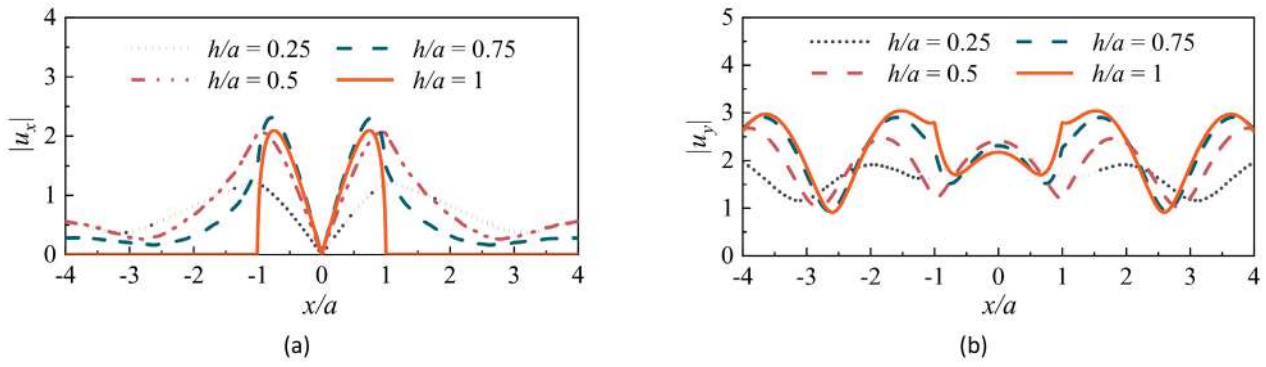

Figure 6 Influence of depth-to-width (h/a) on surface displacement amplitudes for (Sr=0.97) and (θ_{ip1}=0°): (a) |ux|; (b) |uy|.

4.5 *Influence of dimensionless frequency*

Figure 7 presents the surface displacement amplitudes for *Sr*=0.97 as the dimensionless frequency varies from Ω=0.5 to Ω=2.5; the remaining parameters are the same as those in Section 4.2.

As shown in Fig. 7, Ω has a significant influence on the canyon scattering response. At smaller Ω, the displacement curves are relatively smooth and the local peaks are weak. As Ω increases, the curves become more oscillatory, and the number of peaks and troughs increases, indicating a more complex surface response.

For the horizontal displacement amplitude $|u_x|$, larger Ω leads to clearer local peaks and a more evident multi-peak distribution near the canyon. The vertical displacement amplitude $|u_y|$ shows a similar trend. With increasing Ω, the vertical response changes from a smooth pattern to a more strongly oscillatory distribution, suggesting that higher dimensionless-frequency conditions enhance local scattering and amplification near the canyon.

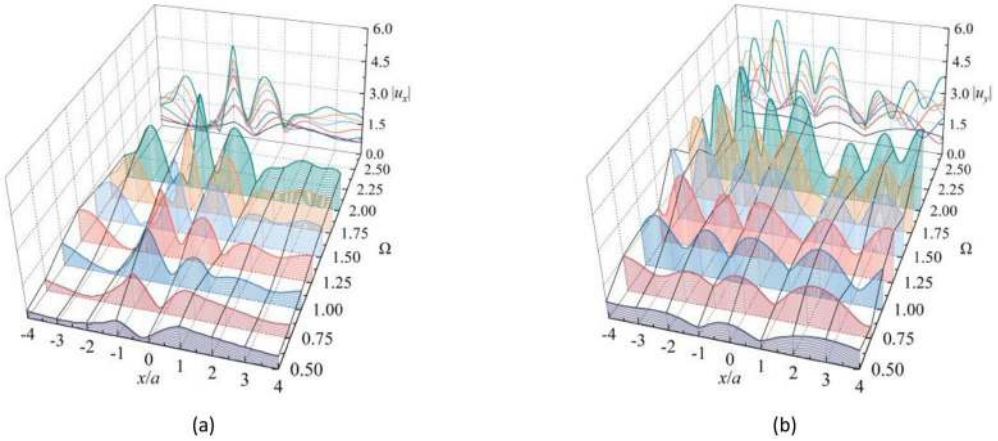

Figure 7 Influence of dimensionless frequency (Ω) on surface displacement amplitudes for Sr=0.97: (a) |ux|; (b) |uy|.

4.6 *Influence of porosity*

Figure 8 presents the surface displacement amplitudes for S_r=0.97 as the porosity *n* increases from 0.05 to 0.45; the other parameters are the same as those in Section 4.2. As shown in Fig. 8, porosity mainly changes the response amplitude rather than the overall spatial pattern. The peak and trough locations remain almost unchanged for different porosity values, indicating that the canyon geometry still dominates the wave-field distribution.

For the horizontal displacement amplitude $|u_x|$, the overall response decreases as *n* increases, especially near the local peaks around the canyon. Under low-porosity conditions, relatively large horizontal peaks appear near the canyon, whereas higher porosity reduces these peaks and makes the curve smoother.

A similar but milder trend is observed for the vertical displacement amplitude $|u_y|$. With increasing *n*, the vertical amplitude and local peaks gradually decrease, and the curve becomes smoother. Compared with the horizontal component, the vertical response remains more stable, suggesting that porosity has a weaker influence on $|u_y|$.

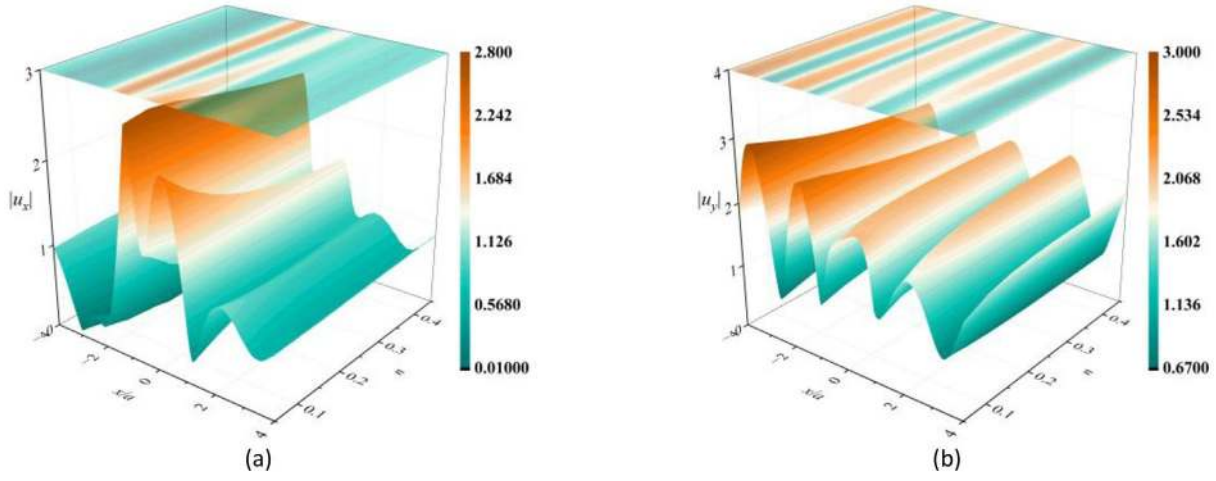

Figure 8 Influence of porosity (n) on surface displacement amplitudes for Sr=0.97: (a) |ux|; (b) |uy|.

4.7 *Comparative analysis of different model assumptions*

Figure 9 compares the surface displacement amplitudes obtained from the nearly saturated poroelastic model (*Sr*=0.97), the single-phase elastic model, and the fully saturated poroelastic model (*Sr*=1.00).

As shown in Fig. 9(a), the three models exhibit similar peak–trough characteristics in the horizontal displacement response near the canyon, but clear differences appear in the amplitude level and local peak positions. The fully saturated model generally gives a weaker horizontal response, whereas the nearly saturated and single-phase elastic models show more pronounced local fluctuations in some regions. This indicates that the canyon geometry controls the main spatial pattern of $|u_x|$, while the medium model affects the local scattering intensity.

For the vertical displacement response in Fig. 9(b), all three models show oscillatory distributions along the ground surface. The peak amplitudes and local response patterns differ among the models, especially near the peak and trough regions. Compared with the fully saturated case, the nearly saturated response is generally stronger, which reflects the influence of occluded gas and the saturation-dependent equivalent bulk modulus of the pore fluid. The difference between the poroelastic and single-phase elastic responses further indicates that solid–fluid coupling can modify the surface displacement response.

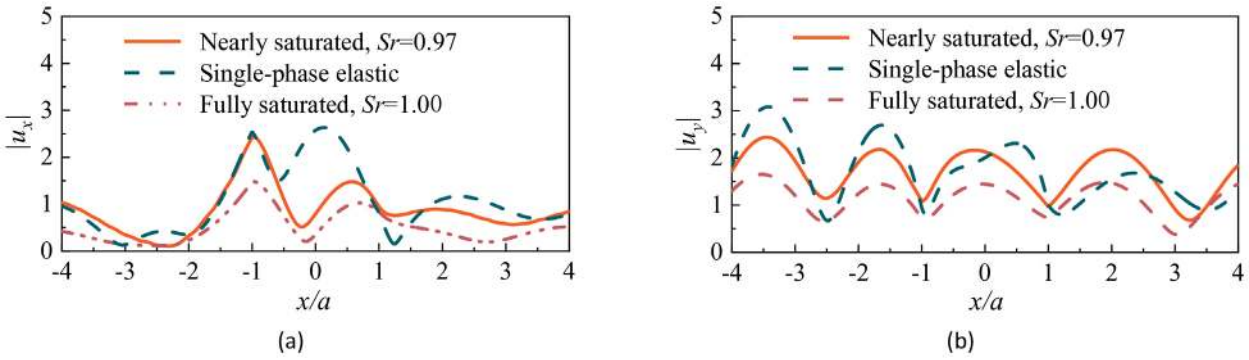

Figure 9 Comparison of nearly saturated, single-phase elastic, and fully saturated models: (a) |ux|; (b) |uy|.

5 Conclusions

An analytical solution is developed for plane P-wave scattering by a circular-arc canyon in a nearly saturated half-space based on the wave theory of nearly saturated porous media, the Fourier–Bessel expansion, and the large-arc approximation. The main contribution of this study is the incorporation of the saturation-dependent equivalent bulk modulus of the pore fluid into topographic-scattering analysis, allowing the influence of near-saturation effects on surface displacement response to be characterized. The formulation is verified by convergence analysis and by reduction to the corresponding saturated case. The effects of saturation, incident angle, depth-to-width ratio, dimensionless frequency, and porosity are examined. The main findings are as follows.

1. Saturation mainly affects the response near full saturation. From *Sr*=0.97 to 0.99, the displacement patterns change little, whereas at *Sr* =1.00, both horizontal and vertical amplitudes decrease markedly, with the horizontal component showing greater sensitivity.

2. The two displacement components respond differently to incident angle. The horizontal component varies non-monotonically in both amplitude and spatial profile, while the vertical component generally decreases as the incident angle increases. Under the same incident angle, the nearly saturated case produces larger amplitudes than the fully saturated case.

3. Increasing *h*/*a* strengthens the canyon effect. The double-peak feature of the horizontal displacement becomes clearer, and the vertical displacement also increases. However, the enhancement tends to level off when the canyon becomes sufficiently deep.

4. Larger values of the dimensionless frequency lead to more oscillatory displacement curves, more frequent peak–trough alternations, and stronger local maxima, indicating enhanced local scattering and amplification near the canyon.

5. Increasing porosity generally weakens the response. Both horizontal and vertical displacement amplitudes decrease, especially near local peaks, while the peak and trough locations change only slightly. This indicates that porosity mainly modifies the response intensity rather than the basic spatial pattern.

Overall, by considering occluded gas and saturation-dependent pore-fluid compressibility, the proposed formulation extends existing elastic and fully saturated poroelastic canyon-scattering models. The results provide a theoretical reference for seismic response evaluation of near-surface canyon sites under nearly saturated conditions.

Acknowledgments

The authors gratefully acknowledge the financial support from the 2026 Gansu Provincial University Teachers Innovation Fund Project, *Study on the Scattering Characteristics of Plane P Waves by a Circular Arc Canyon in Nearly Saturated Soil Sites* (Grant No. 2026B-339), and the Gansu Provincial Soft Science Special Fund Project, *Research on the Mechanism, Pathways and Policies for Empowering the High Quality Development of Gansu Province's Construction Industry through New Quality Productive Forces: An Exploration Based on the Transformation Paradigm of Underdeveloped Regions in Western China* (Grant No. 26JRZE002).

Author's Contributions: Conceptualization, Jin-bo Chen and Bin Hou; Methodology, Jin-bo Chen and Bin Hou; Investigation, Xiang-dong Zhao and Wen-wen Li; Writing--original draft, Jin-bo Chen; Writing--review & editing, Bin Hou and Feng Liu; Resources, Bin Hou and Feng Liu; Supervision, Feng Liu

Data Availability: Research data is only available upon request

Editor: Rogério José Marczak

References

Sanchez-Sesma, F.J. (1987). Site effects on strong ground motion. Soil Dyn Earthq Eng, 6(2), 124–132.

Geli, L., Bard, P.Y., Jullien, B. (1988). The effect of topography on earthquake ground motion: A review and new results. Bull Seismol Soc Am, 78(1), 42–63.

Weber, S., Beutel, J., Häusler, M., et al. (2022). Spectral amplification of ground motion linked to resonance of large-scale mountain landforms. Earth Planet Sci Lett, 578, 117295.

Shi, T., Ma, Q., Zhang, Z. (2026). SV wave scattering by a circular-arc depositional canyon in an unsaturated site. Soil Dyn Earthq Eng, 203, 110132.

Ma, Q., Yang, Y., Zhou, F. (2025a). Study on seismic response of viscoelastic rock layer free field under plane wave incidence under thermal–mechanical coupling effect. Rock Mech Rock Eng, 2025, 1–21.

Li, X. (2026). Three-dimensional finite element modeling of water wave propagation over canyon–cave composite seabed topography. Phys Fluids, 38(1).

Ma, Q., Zhang, M., Zhou, F., et al. (2025b). Analytical analysis of the scattering problem of plane SV waves caused by a circular arc canyon in an unsaturated half-space. Int J Geomech, 25(5), 04025058.

Lee, V.W., Cao, H. (1989). Diffraction of SV by circular canyons of various depth. J Eng Mech ASCE, 115(9), 2035–2056.

Cao, H., Lee, V.W. (1990). Scattering of plane P waves by circular-cylindrical canyons with variable depth-to-width ratio. Soil Dyn Earthq Eng, 9(3), 141–150.

Lee, V.W., Wu, X. (1994). Application of the weighted residual method to diffraction by 2-D canyons of arbitrary shape: II. Incident P, SV and Rayleigh waves. Soil Dyn Earthq Eng, 13(5), 365–375.

Lee, V.W., Liu, W.Y. (2014). Two-dimensional scattering and diffraction of P- and SV-waves around a semi-circular canyon in an elastic half-space: An analytic solution via a stress-free wave function. Soil Dyn Earthq Eng, 63, 110–119.

Biot, M.A. (1956). Theory of propagation of elastic waves in a fluid-saturated porous solid. I. Low-frequency range. J Acoust Soc Am, 28(2), 168–178.

Liu, X., Ma, Q., Zhou, F., et al. (2026). Propagation characteristics of body waves in thermoviscoelastic saturated soil medium based on nonlocal theory. Soil Dyn Earthq Eng, 206, 110261.

Liu, G., Liu, Y., Han, B., et al. (2020). Theoretical and numerical approach for simulating spatially variable seismic underground motions in layered saturated media. J Earthq Eng, 24(4), 601–627.

Feng, G.R., Xu, L.Q. (2025). Theoretical study on the characteristics of P1 wave seismic scattering induced by seabed slope with local interlayers. Soil Dyn Earthq Eng, 190, 109108.

Li, W.H., Zhao, C.G. (2005). Scattering of plane SV waves by cylindrical canyons in saturated porous medium. Soil Dyn Earthq Eng, 25(12), 981–995.

Ba, Z.N., Liang, J.W., Lee, V.W. (2010). Diffraction of plane P waves by a shallow circular-arc canyon in a saturated poroelastic half-space. J Tianjin Univ Sci Technol, 43(6), 523–529.

You, H.B., Liang, J.W., Zhao, F.X. (2011). SV wave scattering by a canyon of arbitrary shape in a saturated layered half-space. Acta Seismol Sinica, 33(6), 735–745.

Huang, L., Liu, Z.X., Wu, C.Q., et al. (2022). A three-dimensional indirect boundary integral equation method for the scattering of seismic waves in a poroelastic layered half-space. Eng Anal Bound Elem, 135, 167–181.

Jin, L., Duan, X., Zhou, Z., et al. (2024). A semi-analytical solution for scattering of incident plane P waves by a saturated river valley with arbitrary shapes containing water. Soil Dyn Earthq Eng, 179, 108566.

Jin, L.J., Duan, X.L., Zhou, B.G., et al. (2023). Surface motion of P/SV wave scattering by a semicircular canyon in saturated half-space by complex function and conformal mapping. Soil Dyn Earthq Eng, 175, 108276.

Zhang, G.X., Yang, Y., Song, Y.Q., et al. (2022). Ground motion around a semi-cylindrical canyon in saturated soil: P-wave incidence. Waves Random Complex Media, 2022, 1–12.

Lainer, M., Müller, G. (2026). A wave based approach for the assessment of fluid–solid coupling for a scattered wave field at an empty canyon. Soil Dyn Earthq Eng, 200, 109827.

Vardoulakis, I., Beskos, D.E. (1986). Dynamic behavior of nearly saturated porous media. Mech Mater, 5(1), 87–108.

Degrande, G., De Roeck, G., Van den Broeck, P., et al. (1998). Wave propagation in layered dry, saturated and unsaturated poroelastic media. Int J Solids Struct, 35(34–35), 4753–4778.

Li, W., Zheng, J., Trifunac, M.D. (2018). Saturation effects on ground motion of unsaturated soil layer-bedrock system excited by plane P and SV waves. Soil Dyn Earthq Eng, 110, 159–172.

Zhang, Y., Ping, P. (2018). Dynamic wave responses near surface in unsaturated porous media. Adv Water Resour, 119, 84–94.

Wang, Y., Gao, G.Y., Yang, J., et al. (2015). The influence of the degree of saturation on dynamic response of a cylindrical lined cavity in a nearly saturated medium. Soil Dyn Earthq Eng, 71, 27–30.

Chen, W., Jeng, D., Chen, W., et al. (2020). Seismic-induced dynamic responses in a poro-elastic seabed: Solutions of different formulations. Soil Dyn Earthq Eng, 131, 106021.

Li, J., Shan, Z., Xie, Z., et al. (2024). Effects of the fluid-porous medium interface on the dynamic response of a nearly saturated seabed under obliquely incident P/SV waves. Soil Dyn Earthq Eng, 182, 108702.

Chang, C.S., Duncan, J.M. (1983). Consolidation analysis for partly saturated clay by using an elastic-plastic effective stress-strain model. Int J Numer Anal Methods Geomech, 7, 39–56.

Ma, Q., Zhou, F., Shao, S., et al. (2023). Diffraction of plane P waves by a circular-arc canyon in an unsaturated poroelastic half-space. Soil Dyn Earthq Eng, 174, 108163.

Yang, J., Wu, S.M., Cai, Y.Q. (1996). Characteristics of propagation of elastic waves in saturated soils. Journal of Vibration Engineering, 9(2), 128–137.